EUCLIPSE

EU Cloud Intercomparison, Process Study & Evaluation Project

Grant agreement no. 244067

Deliverable D3.8 "Development and application of methods to exploit high frequency data for understanding of cloud feedbacks"

Delivery date: Month 36 (Jan 2013)

EUCLIPSE Deliverable D3.8

Development and application of methods to exploit high frequency data for understanding of cloud feedbacks

Mark J. Webb and Adrian P. Lock

Met Office Hadley Centre, FitzRoy Road, Exeter, EX1 3PB, United Kingdom.
Email: mark.webb@metoffice.gov.uk; Tel: +44 (0) 1392 884515.

Introduction

Cloud feedbacks continue to make the largest contribution to inter-model differences in climate sensitivity (Randall et al, 2007, Dufresne and Bony 2008), even when cloud adjustments (Gregory and Webb, 2008, Andrews and Forster 2008) are allowed for (Webb et al 2012, Andrews et al 2012). Understanding the underlying causes of these differences remains a priority. However, the high frequency variability of clouds means that time averaged model output gives a fairly limited picture of the physical mechanisms underlying cloud simulations. High frequency, instantaneous diagnostics are potentially able to give more insight into the physical processes operating and the interactions between them, for example convective intermittency and convective/boundary layer interactions (Zhang and Bretherton, 2008). They also support the diagnosis of any unphysical behaviour related to numerical noise and vertical discretisation effects.

The US Climate Process Team (CPT) on low latitude cloud feedbacks was amongst the first to save high frequency output of this type from GCMs at selected points, and found for example that models could show very different cloud simulations in stratocumulus regions in spite of similar values of net cloud forcing (Bretherton et al 2006). Mapes et al (2009) used these data to relate cloud radiative effects to convective precipitation events, revealing substantial differences in the behaviour of the models' convection schemes. The WGNE-GCSS Pacific Cross Section Intercomparison Project (GPCI, Teixeira et al 2011) saved high frequency data from more than twenty NWP and climate models along a section sampling the stratocumulus regime off the coast of California, the shallow cumulus to the south west and the deep convection in the ITCZ (as well as the transitions between them). They found that the systematic underestimate in cloud fraction in the stratocumulus regimes was in part due to a stratocumulus-to-cumulus transition that occurs too early along the trade wind Lagrangian trajectory, and also noted that some models exhibit a quasi-bimodal structure with cloud cover being either very large or very small, while other models show a more continuous transition.

As part of the second phase of the Cloud Feedback Model Intercomparison Project (CFMIP-2), new cloud feedback experiments were added to the CMIP5 experimental design (Taylor et al 2011), which included additional process diagnostics designed to support investigation of the physical mechanisms underlying cloud feedbacks and adjustments (Bony et al, 2011). These included time-step frequency outputs at 120 locations around the globe, including those analysed by the CPT and GPCI projects, but extended to additionally include various observational sites, and locations with large inter-model differences in cloud feedback (Figure 1,

Table 1). These are included in AMIP experiments forced with observed SSTs which form the basis for +4K global mean SST perturbation experiments. These include one where AMIP SSTs are increased uniformly by 4K (amip4K) and another where a patterned SST perturbation with a global mean of +4K is applied, based on a composite SST response from coupled models in CMIP3 (amipFuture). High frequency outputs are also included in a CO_2 quadrupling experiment with fixed AMIP SSTs designed for the analysis of cloud adjustments (amip4xCO2). These data are now available from several models for each experiment type (Table 2).

Here we present an analysis of the diurnal cycle of cloud feedback in the CFMIP-2 uniform +4K experiments. The primary aims of this analysis are to establish which times of day show the strongest cloud feedbacks, which times of day contribute most to inter-model spread in cloud feedback, and what impact (if any) changes in the diurnal cycle of cloud have on cloud feedback.

Results and Discussion

Relevance of CFMIP locations

To give an indication of the extent to which the CFMIP locations sample the regions which contribute the most to inter-model spread in cloud feedbacks and adjustments, Figure 1 shows maps of ensemble standard deviations of the local cloud feedbacks in the CFMIP-1, CFMIP-2 amip4K and CFMIP-2 amipFuture ensembles, and the cloud adjustments in the CFMIP-2 amip4xCO2 ensemble. The feedbacks and cloud adjustments are diagnosed using the change in the Cloud Radiative Effect (CRE), which quantifies the net radiative impact of cloud changes and the climatological effect of cloud masking on the non-cloud responses (Soden et al, 2004). These are normalised to have global means equal to unity, to support a relative comparison of cloud adjustments and cloud feedbacks. They show that the CFMIP points sample all of the major regimes contributing to inter-model spread in cloud feedback and cloud adjustment, including the subtropical stratocumulus and trade cumulus regions.

Calculation of diurnally resolved quantities

Figure 2 shows diurnally resolved changes in the shortwave and longwave CRE between the AMIP and AMIP+4K experiments averaged over the CFMIP-2 ocean locations (see Table 1). The change in CRE can in this case be considered a measure of the cloud feedback for comparison purposes because all of the models are subject to the same SST increase. For each of the 119 locations available from all six models, we calculated the 30 year climatological annual mean changes for each time of day (UTC). We then rotated the time coordinates for each location to align the times of the maximum solar insolation, placing these at 12 noon (mean solar time) before averaging across locations. Radiative fluxes are only available every three hours from CNRM-CM5, which means that the diurnal cycle is less well resolved, and the time of the maximum insolation is less accurately diagnosed. Shortwave radiative fluxes are not yet available from EC-EARTH which precludes this model from our current analysis, although it will be included in the future.

Time of largest shortwave CRE response

Figure 2(a) shows that the models show a range of shortwave CRE responses varying from weakly negative to positive, as seen in many previous studies. If there was no change in the diurnal cycle of the cloud properties (i.e. cloud properties changed by the same amount at all times of day) then we would expect the shortwave CRE responses to be symmetric about a maximum at solar noon, with a diurnal cycle following the solar insolation but with different magnitudes depending on the size of the diurnal mean change in cloud properties. The majority of models show only modest deviations from this situation, suggesting that changes in the diurnal cycle of cloud properties are generally small compared to changes in diurnal mean quantities. Figure 3(a,b) confirms that this is generally the case for low cloud fraction and cloud liquid water path. CanAM4 is the exception to this however. Although its shortwave CRE response peaks with a positive value in the morning, a negative local minimum is present in the afternoon which is unusual compared to the other models (Figure 2(a)). We attribute this behaviour to the fact that CanAM4 has an unusually large change in the diurnal cycle of its low cloud fraction relative to the size of the change in its diurnal mean (Figure 3(a)).

Most of the models show the largest shortwave CRE response in the morning (Figure 2(a)), which means that cloud properties must be changing more at that time than at midday. Low level cloud fraction reduces in all of the models at all times of day over the oceans (Figure 3(a)), and the models which have stronger shortwave CRE responses in the morning show larger decreases in low cloud fraction at that time than at midday. MRI-CGCM3 is the exception, with the largest positive changes in shortwave CRE around and soon after noon, and the largest decreases in low cloud fraction in the afternoon. The tendency for the models to show the largest shortwave CRE response in the morning results in the inter-model spread also being largest at that time.

Relative impact of low cloud fraction and liquid water path changes

The liquid water path increases in most of the models, the exception being HadGEM2-A, which shows a small decrease (Figure 3(b)). This slightly unusual behaviour in HadGEM2-A may be related to the nature of its PDF based cloud scheme which has a strong coupling between cloud fraction and cloud water content. The increases in the majority of models would on their own result in a negative shortwave CRE response, but in most cases they are not large enough to overcome the positive response due to the reductions seen in the low cloud amounts. For example, IPSL-CM5-LR shows a 23% reduction in diurnal mean low cloud fraction relative to its control value, while its liquid water path increases by just 7% (Figure 3(c,d)). These results are consistent with the findings of Zelinka et al (2013), who show that cloud optical depth does generally increase in the warmer climate in models, but that the effect of this on the shortwave cloud CRE response is more than compensated for by reductions in cloud fraction. CNRM-CM5 is an exception to this however; it has the largest increase in cloud liquid water and one of the smallest reductions in low cloud fraction, which presumably explains its weakly negative shortwave CRE response.

The diurnal variations of the present-day values of liquid water path about the mean tend to be in phase with those of the low cloud fraction (Figure 3(c,d)), which is consistent with observations (Wood et al, 2002). The diurnal variations of the low

cloud and liquid water path responses also tend to be in phase in most models, but CNRM-CM5 is an exception to this, with the largest liquid water path increase occurring in the morning rather than the afternoon (Figure 3(a,b)).

Present-day diurnal cycle in marine low cloud properties

Why do the models generally show the largest changes in marine low-cloud properties in the mornings? Observations show that oceanic stratocumulus clouds tend to form overnight and then break up through the day as the cloud layer is heated by solar absorption. For example, Wood et al (2002) showed that cloud liquid water paths retrieved from the Tropical Rainfall Measuring Mission Microwave Imager over the tropical and subtropical oceans tend to peak in the early morning. If the models capture this behaviour, it is conceivable that smaller cloud amounts later in the day mean that there is less cloud to break up, resulting in a weaker cloud feedback. Figure 3(c,d) shows that the models do a remarkably good job of capturing the observed phase in the diurnal cycle; all have a maximum low cloud fraction and liquid water path in the morning and a minimum at or after solar noon, and this is reflected in present-day values of the shortwave CRE which are most negative before 12 noon (Figure 2(c)). Wood et al (2002) find that diurnal amplitudes in liquid water path are observed which are considerable fractions of the mean, reaching as much as 15-35% in coastal stratocumulus regions. There are however large differences in amplitude between the models; CanAM4 has the largest diurnal amplitude in liquid water path, and its amplitude is 43% the size of its diurnal mean, somewhat larger than observed. MRI-CGCM3 has the smallest, at 13%.

Diurnal cycle in longwave CRE over the oceans

Figure 2 shows that over the oceans the diurnal cycle in the longwave CRE and its response to a +4K perturbation is much smaller than that in the shortwave. The models mostly show minima in the longwave CRE response around or before noon (Figure 2(b)), generally coinciding with minima in the high cloud response (Figure 4(a)). This is consistent with the expectation that deep convection over the oceans is slightly suppressed during the daytime because of atmospheric stabilisation due to enhanced shortwave heating. CanAM4 is an exception in that it shows a minimum longwave CRE response centred near early afternoon, which is at a time when both the high cloud and ice water path responses are weakening. There is no obvious relationship across the models between the changes in the diurnal cycle of these quantities and their present-day diurnal cycles. However, it is perhaps worth noting that the models with the strongest diurnal cycles in their high-cloud responses (MPI-ESM-LR and CNRM-CM5) are also those that have the most high cloud in the present day (Figure 4(a,c)). Also the model with the smallest present-day high cloud fraction (HadGEM2-A), has the smallest diurnal cycle in the high cloud response. CanAM4 is slightly unusual compared to the other models in that is has a local maximum in longwave CRE over the ocean points in its present-day simulation. We attribute this effect to the inclusion of near-infrared solar radiation with wavelengths above 4 microns in the longwave radiation diagnosed from CanAM4 (Li et al, 2010).

The diurnally varying components of the longwave CRE responses discussed above are small compared to the inter-model differences present in the diurnal meaned responses (Figure 2(b)). MRI-CGCM3 shows a reduction in longwave CRE, with relatively neutral changes in ice water path and high cloud fraction (Figure

4(a,b)), which would be consistent with the reduction in longwave CRE in this model mainly being a cloud masking effect. CanAM4 has the largest increase in high cloud fraction and one of the largest increases in ice water path, consistent with it having the strongest longwave CRE increase. These upper level cloud changes in CanAM4 would also be expected to make the shortwave CRE response less negative, and this might explain the relatively small diurnally meaned shortwave CRE response in this model given its somewhat typical changes in diurnal mean low cloud properties. The other models show diurnally meaned changes in high cloud fraction and/or ice water path consistent with more neutral longwave CRE responses.

Diurnal cycle over land points

Figure 5(c) shows that the diurnal cycle in present-day shortwave CRE over land points is generally more symmetric than that seen over the ocean points (cf Figure 2(c)); this can be explained by present-day diurnal cycles in low and high cloud fraction which are generally smaller over land than ocean (see Figure 6(c) cf Figure 3(c) and Figure 7(c) cf Figure 4(c)). Although smaller in amplitude, the majority of the models show a quite similar diurnal cycle in low cloud properties over the land compared to the ocean, with maxima in the morning and minima in the afternoon (Figure 6(c) cf Figure 3(c)). HadGEM2-A and CNRM-CM5 are exceptions however, with local maxima in low cloud amount and liquid water path later in the day, presumably related to deep convective activity.

We would expect the diurnal cycle of high cloud to be quite different over land compared to ocean, the result of deep convection building up through the day in response to increasing land surface temperatures. The models tend to show a minimum in present-day longwave CRE in the mornings and a maximum around mid-afternoon, which is consistent with this expectation (Figure 5(d)). High cloud fraction and ice water path values tend to be smallest in the morning, rising to their maximum values in the afternoon (Figure 7(c,d)). The amplitudes of the diurnal variations in the longwave CRE are mostly small compared to the diurnal mean. CNRM-CM5 shows a diurnal cycle in present-day longwave CRE which is slightly stronger than the majority of the models (Figure 5(d)); we attribute this to a slightly stronger diurnal cycle in high cloud fraction and ice water path (Figure 7(c,d)). HadGEM2-A however has an unusually large diurnal cycle in longwave CRE which is not apparent in the high cloud fraction or ice water path. We attribute this behaviour to an adjustment which is made to the outgoing longwave radiation in HadGEM2-A to improve the diurnal cycle of surface temperature. In HadGEM2-A and earlier versions of the Met Office model, the radiation code is called every three hours. This limits the ability of the land surface to emit more longwave radiation with increasing temperatures between radiation time steps, resulting in an unrealistically large diurnal cycle in surface temperature. For this reason the additional surface emission due to changes in surface temperature between radiation time steps is estimated and radiated to space via an adjustment to the outgoing longwave radiation. This adjustment is not applied to the clear-sky outgoing longwave radiation however, resulting in an exaggerated diurnal cycle in the diagnosed longwave CRE. This could be corrected for in future by using all-sky and clear-sky longwave fluxes which are adjusted consistently.

The shortwave CRE response to the +4K SST perturbation is much smaller over land than ocean in the majority of models (Figure 5(a) cf Figure 2(a)). CNRM-CM5 is an exception to this, with a strong negative shortwave CRE response over land, which we attribute to a strong increase in cloud liquid water path combined with

a relatively small decrease in low cloud fraction (Figure 6(a,b)). The strongest shortwave CRE responses are in the morning in IPSL-CM5-LR and CanAM4, and in the afternoon in HadGEM2-A and MPI-ESM-LR. The responses in MRI-CGCM3 and CNRM-CM5 are largest around noon. The times of the maximum longwave CRE response are equally diverse (Figure 5(b)). This is a less coherent picture than that seen over the ocean which may reflect the diversity of deep convection schemes used in climate models. This also suggests that the behaviour of deep convection schemes in the present day is not a good guide to how they will respond in the warming climate.

Conclusions and Future Work

Here we have examined the diurnal cycle of clouds and cloud feedbacks using high frequency outputs from six CFMIP models. The models capture the observed phase of the diurnal cycle in low cloud properties over the oceans, although the amplitude of this variation varies and is in some cases larger relative to the diurnal mean than is the case in observations. The fact that the models all capture this suggests that the mechanism is likely to be quite simple; one possibility is that increased solar absorption by clouds during the day heats the cloud layer, reducing relative humidity and hence cloud fraction.

The models tend to show larger changes in low cloud properties in the warmer climate in the morning when more low cloud is present in the control. This results in shortwave cloud feedbacks being strongest and having the largest inter-model spread at this time of day. This suggests that careful comparisons with observations might help to constrain future model predictions of changes in the diurnal cycle of low clouds. However, this is unlikely to have a large impact of inter-model spread in cloud feedback, which is mainly explained by differing responses in diurnally meaned cloud properties, rather than changes in the diurnal cycle.

A number of unusual behaviours have been noted in individual models. We would like to analyse these in more detail in future work, to establish which models are representing key processes unusually well or unusually badly. We consider an improved understanding of such behaviours in models to be a necessary pre-requisite for reducing uncertainty in future model predictions.

An obvious next step is to extend this analysis to additional models as they become available, and also to apply it to the other CFMIP-2 experiments, for example in the context of cloud adjustments and in idealised aquaplanet configurations. Examination of the diurnal cycle is but one application of these high frequency model outputs. Many other questions remain which can be investigated using these data. They can be used to refine large scale forcings used to run LES models in cloud feedback studies such as CGILS (The CFMIP-GCSS Intercomparison of LES and SCMs, Zhang et al (2013)). They can be used to separate cloud feedback into contributions from times when convection is dominant from those when turbulent boundary layer processes are dominant. More generally, relationships between clouds and other model variables such as surface fluxes, temperature and humidity profiles and their tendency terms can be investigated. One advantage of these outputs is that the order of events can potentially be used to determine causality in a way that is not possible with time meaned outputs. Moreover these model outputs constitute a rich database of model behaviour against which physical hypotheses on cloud feedback mechanisms can be tested.

Acknowledgements

This work was supported by the Joint DECC/Defra Met Office Hadley Centre Climate Programme (GA01101). The research leading to these results has received funding from the European Union, Seventh Framework Programme (FP7/2007-2013) under grant agreement number 244067 via the EU CLoud Intercomparison and Process Study Evaluation project (EUCLIPSE). We acknowledge the World Climate Research Programme's Working Group on Coupled Modelling, which is responsible for CMIP, and we thank the climate modelling groups for producing and making available their model output. For CMIP the U.S. Department of Energy's Program for Climate Model Diagnosis and Intercomparison provides coordinating support and led development of software infrastructure in partnership with the Global Organization for Earth System Science Portals. We would like to acknowledge in particular Philip Bentley, Alejandro Bodas-Salcedo, Sandrine Bony, Jason Cole, Herve Douville, Jean-Louis Dufresne, Hideaki Kawai, Jamie Kettleborough, Tsuyoshi Koshiro, Carlo Lacagnin, Marc Salzmann, Frank Selten, Yoko Tsushima, Sophie Tyteca, and Jonny Williams for their efforts in preparing time series outputs from the models.

References

Andrews, T., and P.M. Forster (2008), CO_2 forcing induces semi-direct effects with consequences for climate feedback interpretations. Geophys. Res. Lett., **35**, L04802, doi:10.1029/2007GL032273.

Andrews, T., J. M. Gregory, M. J. Webb, and K. E. Taylor (2012), Forcing, feedbacks and climate sensitivity in CMIP5 coupled atmosphere-ocean climate models, Geophys. Res. Lett., **39**, L09712, doi:10.1029/2012GL051607.

Bony, S., et al. (2011), CFMIP: Towards a better evaluation and understanding of clouds and cloud feedbacks in CMIP5 models. Clivar Exchanges, **56**, 16, 2.

Bretherton CS (2006), The climate process team on low-latitude cloud feedbacks on climate sensitivity. US Clivar Variations **4**:7–12.

Dufresne, Jean-Louis, Sandrine Bony (2008), An Assessment of the Primary Sources of Spread of Global Warming Estimates from Coupled Atmosphere–Ocean Models. J. Climate, **21**, 5135–5144.

Gregory, J.M. and M.J. Webb (2008), Tropospheric adjustment induces a cloud component in CO_2 forcing. J. Climate, **21**, 58-71, doi :10.1175/2007JCLI1834.1.

Li, J., Curry, C. L., Sun, Z. and Zhang, F. (2010) Overlap of Solar and Infrared Spectra and the Shortwave Radiative Effect of Methane. Journal of the Atmospheric Sciences, 2010, **67**, 2372-2389.

Mapes BE, Bacmeister J, Khairoutdinov M, Hannay C, Zhao M (2009), Virtual field campaigns on deep tropical convection in climate models. J. Climate **22,**244–257. doi:10.1175/2008JCLI2203.1

Randall DA, Wood RA, Bony S, Colman R, Fichefet T, Fyfe J, Kattsov V, Pitman A, Shukla J, Srinivasan J, Stouffer RJ, Sumi A, Taylor KE (2007) Climate models and their evaluation. In: Solomon S, Qin D, Manning M, Chen Z, Marquis MC, Avery KB, Tignor M, Miller HL (eds) Climate Change 2007: The physical science basis. Contribution of Working Group I to the fourth assessment report of the intergovernmental panel on climate change, 589–662, Cambridge University Press.

Soden, B. J., A. J. Broccoli, and R. S. Hemler, (2004), On the use of cloud forcing to estimate cloud feedback. J. Climate, **17**, 3661–3665.

Taylor, K.E., R.J. Stouffer and G.A. Meehl (2011), An overview of CMIP5 and the experiment design. Bull. Amer. Meteor. Soc., doi:10.1175/BAMS-D-11-00094.1.

Teixeira, J., and Coauthors, (2011), Tropical and Subtropical Cloud Transitions in Weather and Climate Prediction Models: The GCSS/WGNE Pacific Cross-Section Intercomparison (GPCI). J. Climate, **24**, 5223–5256. doi: http://dx.doi.org/10.1175/2011JCLI3672.1

Webb, M. J. and Lambert, F. H. and Gregory, J. M. Origins of differences in climate sensitivity, forcing and feedback in climate models, (2012) Clim. Dyn. (Online First) 10.1007/s00382-012-1336-x

Wood, R., Bretherton, C. S. and Hartmann, D. L. (2002), Diurnal cycle of liquid cloud water path over the subtropical and tropical oceans. Geophysical Research Letters, **29**, 2092-2095.

Zelinka, M.D., S.A. Klein, K.E. Taylor, T. Andrews, M.J. Webb, J.M. Gregory, and P.M. Forster, 2013: Contributions of Different Cloud Types to Feedbacks and Rapid Adjustments in CMIP5. In press, J. Climate. doi: 10.1175/JCLI-D-12-00555.1.

Zhang M., C. S. Bretherton, (2008) Mechanisms of low cloud climate feedback in idealized single-column simulations with the community atmospheric model (CAM3). J. Climate, **21**,4859–4878. doi:10.1175/2008JCLI2237.1

M. Zhang, C. S. Bretherton, P. N. Blossey, S. Bony, F. Brient and J.-C. Golaz, 2013. The CGILS Experimental Design to Investigate Low Cloud Feedbacks in General Circulation Models by Using Single-Column and Large-Eddy Simulation Models. In press, J. Adv. Model. Earth Syst., doi:10.1029/2012MS000182

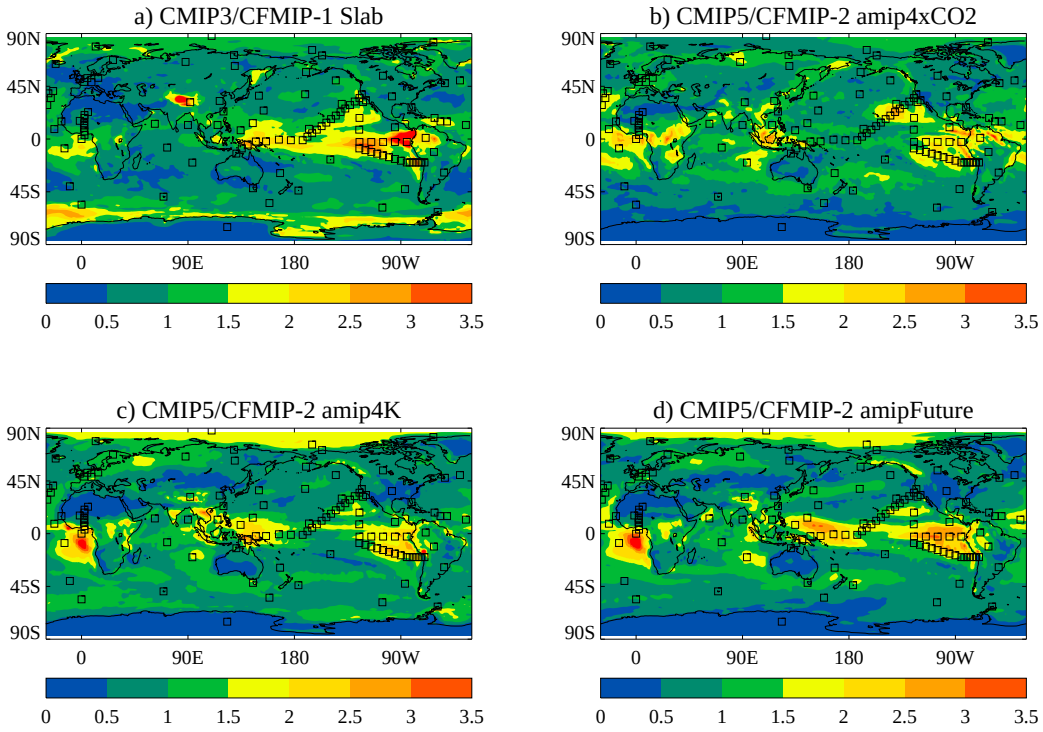

Figure 1. CFMIP time series output locations. The maps show the relative contributions of difference parts of the globe to inter model spread in (a) cloud feedbacks from CFMIP-1, (b) cloud adjustments in CFMIP-2 and (c,d) cloud feedbacks in CFMIP-2. The maps show local standard deviations across each ensemble, normalised to the same global mean. The squares show the locations of the CFMIP-2 high frequency outputs.

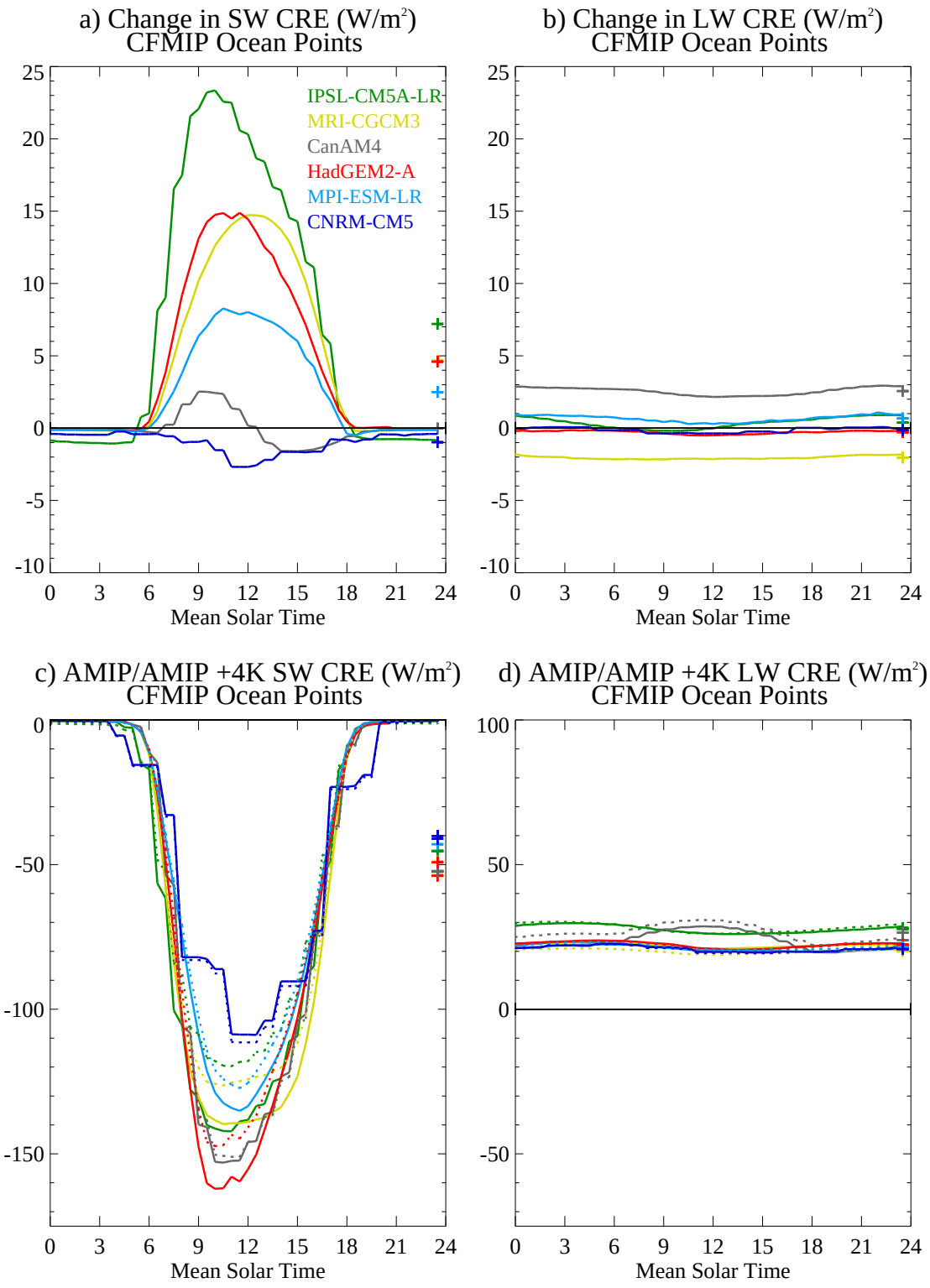

Figure 2. Diurnal cycle of the Cloud Radiative Effect (CRE) averaged over CFMIP-2 ocean locations in CFMIP-2/CMIP5 AMIP and uniform +4K perturbation experiments. a) and b) show responses in the shortwave and longwave CRE respectively to the uniform +4K SST perturbation. c) and d) show the shortwave and longwave values in the AMIP (solid) and AMIP + 4K (dashed) experiments. + symbols indicate the diurnal mean values.

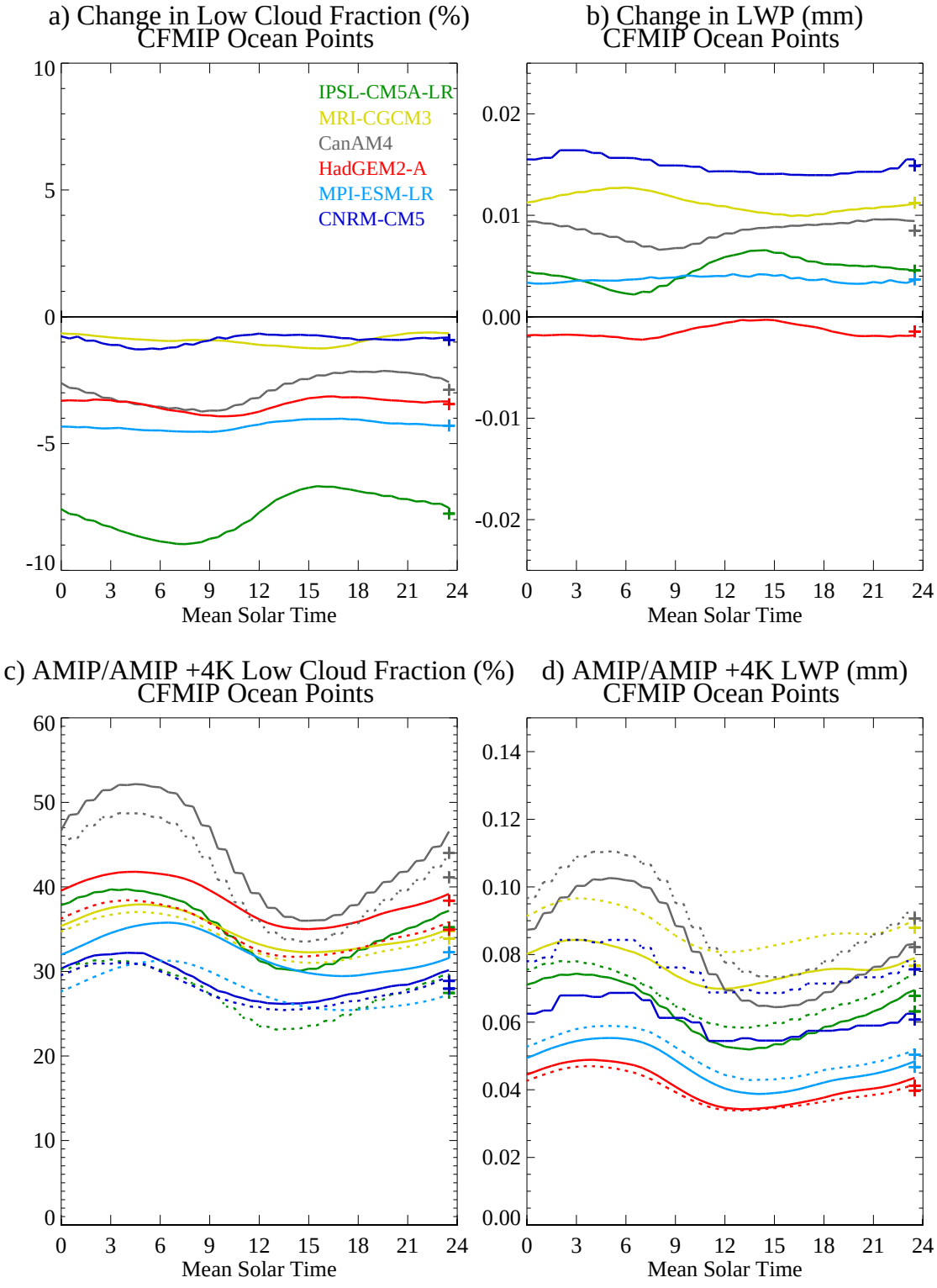

Figure 3. As Figure 2, but for low cloud fraction and liquid water path. The low cloud fraction is calculated by taking the maximum cloud fraction below 640hPa.

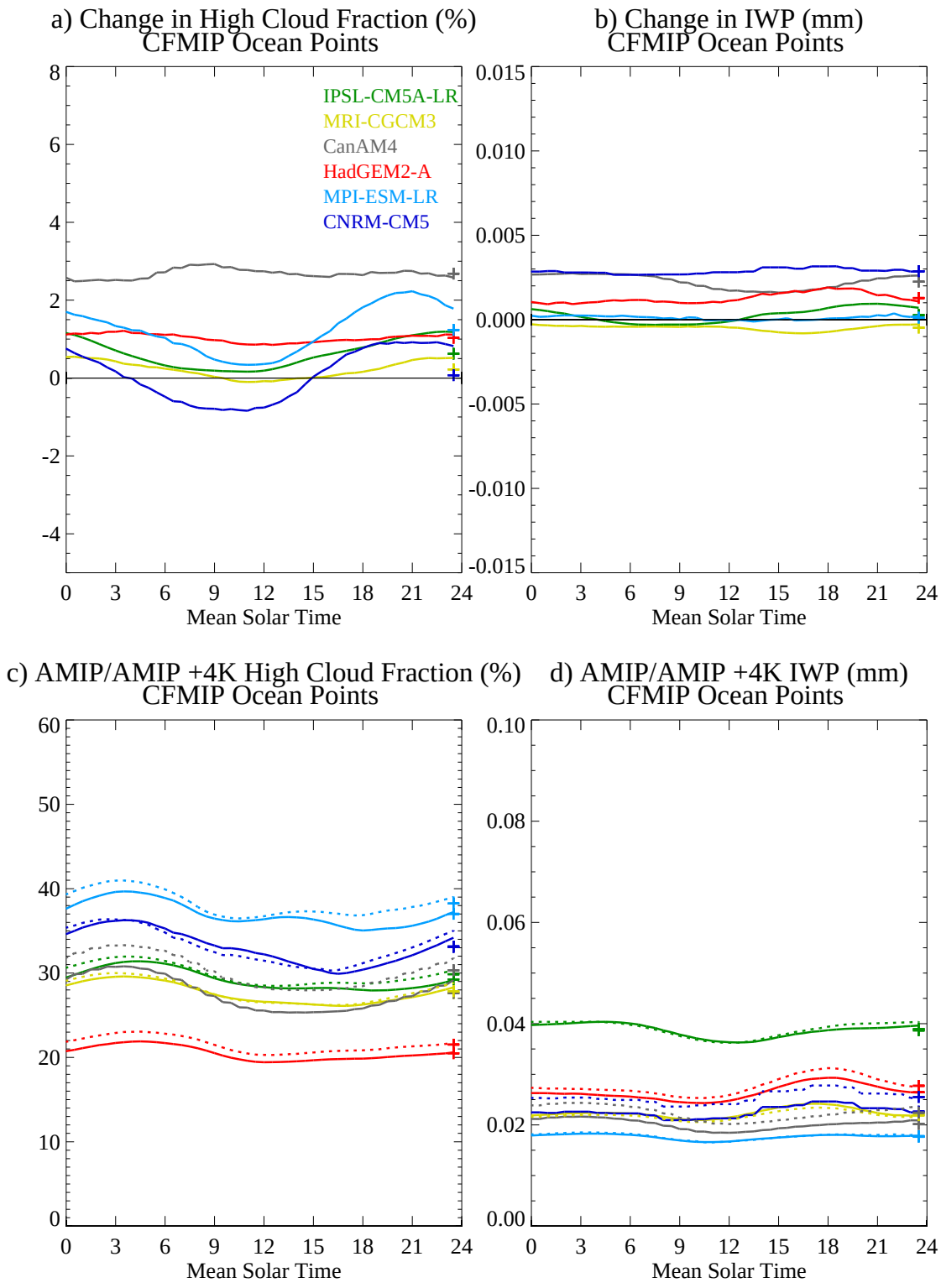

Figure 4. As Figure 2, but for high cloud fraction and ice water path. The high cloud fraction is calculated by taking the maximum cloud fraction above 440hPa.

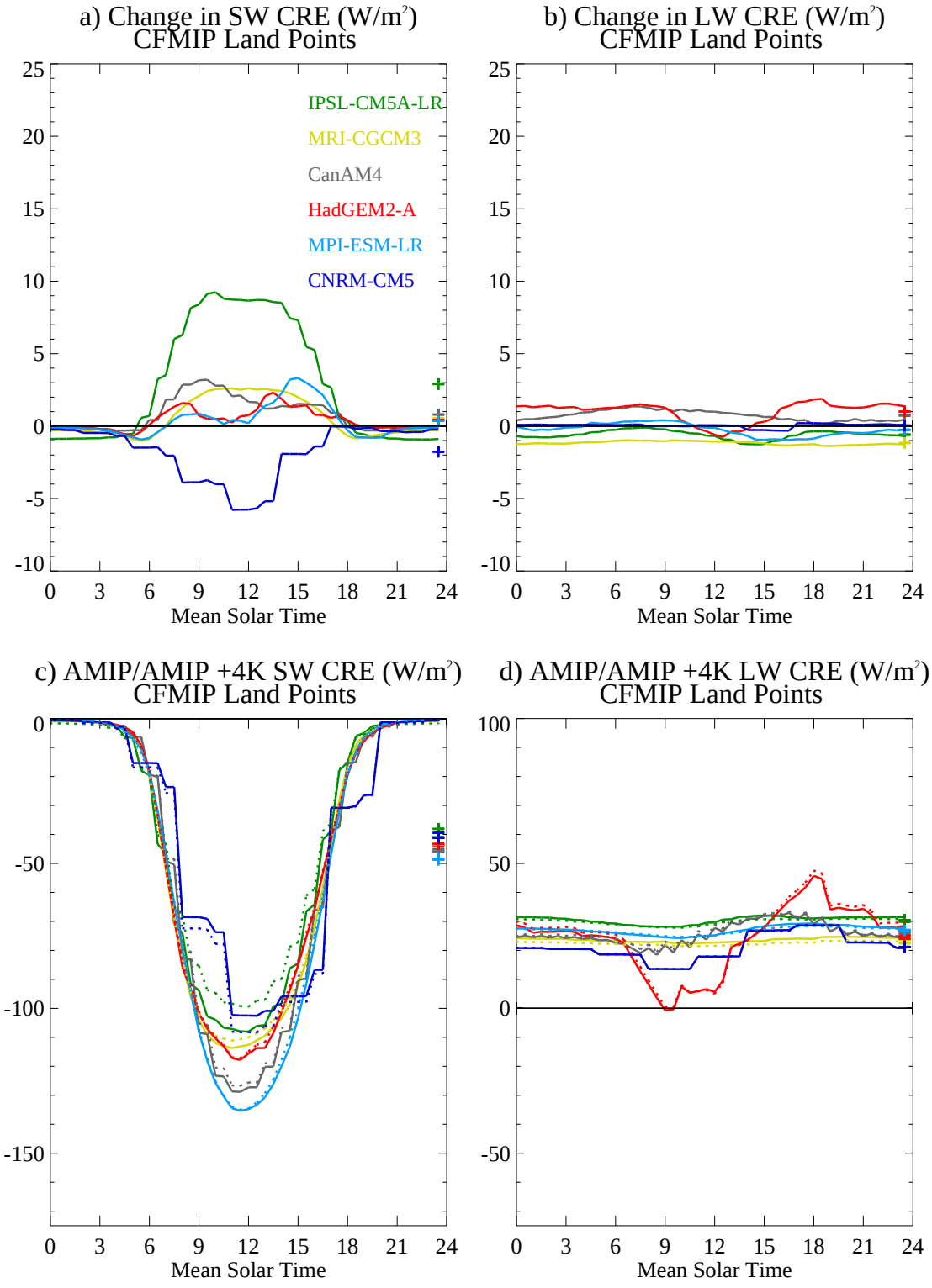

Figure 5. As Figure 2, but for land points.

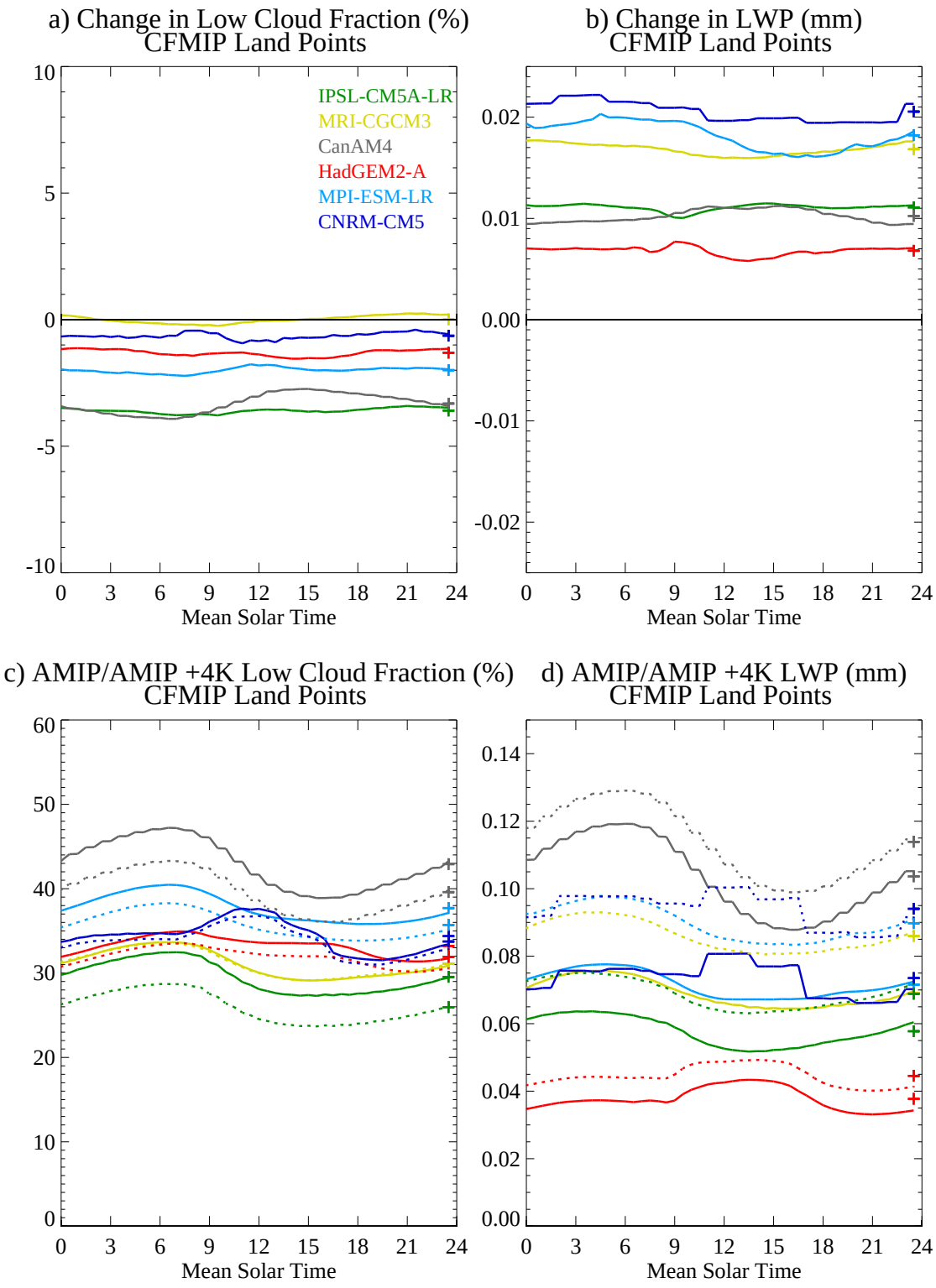

Figure 6. As Figure 3, but for land points.

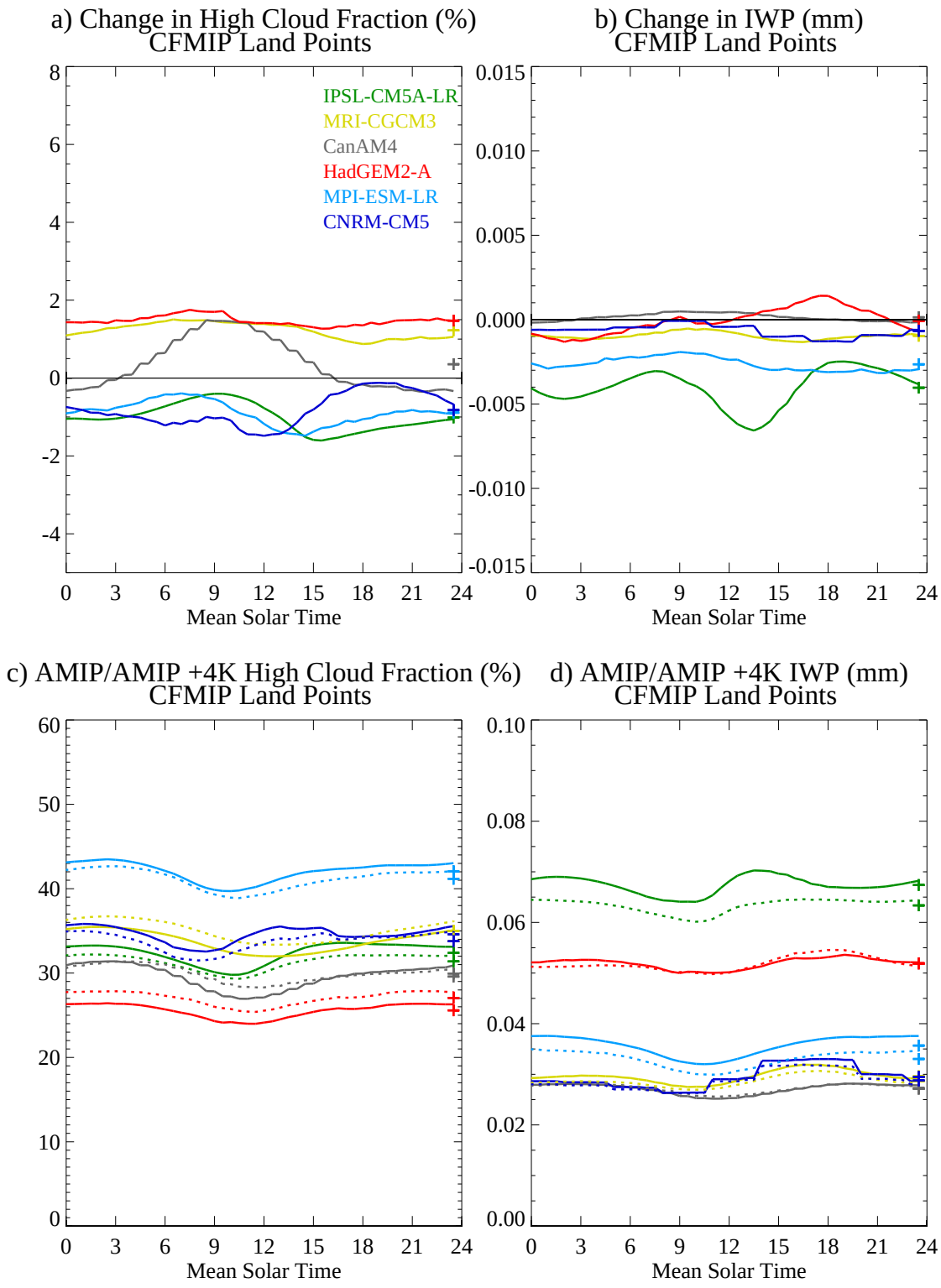

Figure 7. As Figure 4, but for land points.

Table 1(a): Locations of CFMIP point outputs. Land points are shown in bold.

	Lon	Lat	Description (Source)
1	**290**	**-20**	**VOCALS cross section (Rob Wood)**
2	287.5	-20	"
3	285	-20	"
4	282.5	-20	"
5	280	-20	"
6	277.5	-20	VOCALS cross section (Rob Wood)
7	275	-20	85W 20S WHOI SE Pacific stratus buoy (http://uop.whoi.edu/stratus/) (CPT)
8	270	-18.5	SouthEast Tropical Pacific Section (CFMIP)
9	265	-17	"
10	260	-15.5	"
11	255	-14	"
12	250	-12.5	"
13	245	-11	"
14	240	-9.5	"
15	234.9	-8	125.1W 8S central Pacific SE trades TAO buoy (CPT)
16	**-123**	**38.1**	**Point Reyes ARM Mobile Facility N38 5.51 W122 57.33 (AMF)**
17	235	35	GCSS Pacific cross section (GPCI) (Joao Teixeira)
18	231	32	"
19	227	29	"
20	223	26	"
21	219	23	"
22	215	20	"
23	211	17	"
24	207	14	"
25	203	11	"
26	199	8	"
27	195	5	"
28	191	2	"
29	187	-1	GCSS Pacific cross section (GPCI) (Joao Teixeira)
30	177	-1	GPCI/Tropical West Pacific link point (CFMIP)
31	166.9	-0.5	166.9E 0.5S Nauru ARM (CPT)
32	156	-2	156E 2S COARE (CPT)
33	147.4	-2.1	147.4E 2.1S Manus ARM (CPT)
34	**140.5**	**-4.75**	**Papua New Guinea (CFMIP)**
35	135.5	-8	Arafura Sea (CFMIP)
36	**130.9**	**-12.4**	**130.9E 12.4S Darwin ARM (CPT)**
37	**-97.5**	**36.4**	**97.5W 36.4N Oklahoma ARM (CPT)**
38	**-156.6**	**71.3**	**156.6W 71.3N Barrow ARM (CPT)**
39	**-62**	**-11**	**62W 11S Amazonia (CPT)**
40	**4.9**	**52**	**4.93E 51.97N Cabaaw Mast Netherlands (CPT)**

Table 1(b): Locations of CFMIP point outputs (continued).

	Lon	Lat	Description (Source)
41	**145**	**-42**	**145E 42S Cape Grim Tasmania (CPT)**
42	-51	15	51W 15N WHOI Atlantic tradewind NTAS buoy (http://uop.whoi.edu/ntas/) (CPT)
43	-140	30	140W 30N OWS N (CPT)
44	-145	50	145W 50N OWS P (CPT)
45	-125.2	8	125.2W 8N central Pacific ITCZ TAO buoy (CPT)
46	120	23.5	120E 23.5N China Sea (CPT)
47	**-28**	**39**	**Graciosa in the Azores (28W 39N) 2009 AMF deployment (Chris Bretherton)**
48	**8.4**	**48.5**	**AMF Black forest Germany Main Site: N48 32.403 E08 23.812 (AMF)**
49	**116.8**	**32.5**	**AMF Shouxian China Location: 32 33N 116 46E (AMF)**
50	**129.6**	**62.3**	**CEOP 2 Eastern Siberian Tiaga 62.3N 129.6E (Martin Koehler)**
51	**91.9**	**31.4**	**CEOP 5 Tibet 31.4N 91.9E (Martin Koehler)**
52	134.5	7.5	CEOP 10 Western Pacific Ocean 7.5N 134.5E (Martin Koehler)
53	**14.1**	**52.2**	**CEOP 26 Lindenberg 52.2N 14.1E (Martin Koehler)**
54	**26.6**	**67.4**	**CEOP 27 Sodankyla 67.4N 26.6E (Martin Koehler)**
55	**-105.1**	**54**	**CEOP 33 BERMS (CliC) 54.0N 105.1W (Martin Koehler)**
56	**-62.5**	**82.5**	**CEOP 34 Alert Nunavut 82.5N 62.5W (Martin Koehler)**
57	**-53.4**	**-28.6**	**CEOP 48 Cruz Alta (LPB) 28.6S 53.4W (Martin Koehler)**
58	-24	41	ASTEX (41N 24W) (Adrian Lock)
59	-26	35	ASTEX (35N 26W) (Adrian Lock)
60	-29	29	ASTEX (29N 29W) (Adrian Lock)
61	-35	12	ATEX = 12N 35W (Adrian Lock)
62	-56.5	15	BOMEX = 15N 56.5W (Adrian Lock)
63	-61.5	18	RICO = 18N 61.5W (Adrian Lock)
64	-119.5	33	EUROCS/FIREI = 33N 119.5W (Adrian Lock)
65	-122	31.5	DYCOMSII = 31.5N 122W (Adrian Lock)
66	-85	-2.5	East Pacific Point (CFMIP)
67	-95	-2.5	East Pacific Point (CFMIP)
68	-105	-2.5	East Pacific Point (CFMIP)
69	-115	-2.5	East Pacific Point (CFMIP)
70	-125	-2.5	East Pacific Point (CFMIP)
71	-125	18	East Pacific Point (CFMIP)
72	**-69**	**1**	**North West of Amazonia (CFMIP)**
73	62	13	MONSOON INFLOW (CFMIP)
74	**-14.4**	**-7.97**	**ASCENSION IS./WIDEAWAKE (RATPAC) (CFMIP)**
75	150	37	Kurishio region (CFMIP)
76	-21.9	64.1	64.1285N 21.9407W Reykjavik (CFMIP)
77	**-170.2**	**57.15**	**ST. PAUL ISLAND (RATPAC) (CFMIP)**
78	**-58.9**	**-62.2**	**BELLINGSHAUSEN (RATPAC) (CFMIP)**
79	**11.95**	**78.93**	**BSRN site Svalbard (CFMIP)**
80	**144.8**	**13.6**	**Guam (CFMIP)**

Table 1(c): Locations of CFMIP point outputs (continued).

	Lon	Lat	Description (Source)
81	**69.3**	**-49.2**	**Southern Ocean - Kerguelen Islands (CFMIP)**
82	**158.9**	**-54.6**	**Southern Ocean - Macquarie Island (CFMIP)**
83	**-81**	**27**	**Florida (81W 27N) (Brian Mapes)**
84	**-167.7**	**8.7**	**Kwajalein (167.7W 8.7N) (Brian Mapes)**
85	90	12	JASMINE (90E 12N) (Brian Mapes)
86	115	12	SCS (115E 12N) (Brian Mapes)
87	-95	10	EPIC (95W 10N) (Brian Mapes)
88	-23	8.5	GATE (23W 8.5N) (Brian Mapes)
89	**-1.44**	**51.14**	**Chilbolton UK 51.1445 North 1.4370 West altitude 80 m. (Robin Hogan)**
90	**2.2**	**48.71**	**SIRTA Palaiseau (Paris) France 48.713 North 2.204 Est (Cloudnet)**
91	93.7	-20.1	CFMIP West of Australia
92	254.4	-58.5	CFMIP Southern Ocean
93	**-52.75**	**47.67**	**CFMIP ST. JOHNS (RATPAC)**
94	**-176.6**	**-43.95**	**CFMIP CHATHAM ISLAND (RATPAC)**
95	**72.4**	**-7.3**	**CFMIP DIEGO GARCIA (RATPAC)**
96	**-9.88**	**-40.35**	**GOUGH IS. (RATPAC) (CFMIP)**
97	189.1	38.2	CFMIP Central North Pacific
98	**-149.6**	**-17.5**	**CFMIP Tahiti 17.5S 149.6W**
99	0	-56	CFMIP South Atlantic
100	273.5	-42.7	CFMIP off coast of Chile
101	**153.97**	**24.3**	**MARCUS IS. (RATPAC) (CFMIP)**
102	**167.9**	**-29.03**	**NORFOLK ISLAND (RATPAC) (CFMIP)**
103	-40	50	CFMIP North West Atlantic
104	**87.95**	**65.78**	**TURUKHANSK (RATPAC) RS**
105	0	0	0. 0.N Pirata Buoy (AMMA Francoise Guichard)
106	2.5	3.5	2.5 3.5N (AMMA Francoise Guichard)
107	**2.5**	**6.5**	**2.5 6.5N (AMMA Francoise Guichard)**
108	**2**	**9.5**	**2. 9.5N Oueme (AMMA Francoise Guichard)**
109	**2.5**	**11.5**	**2.5 11.5N (AMMA Francoise Guichard)**
110	**2.2**	**13.5**	**13.5N 2.2E Niamey ARM Mobile Facility (AMF)**
111	**-1.5**	**15.5**	**-1.5 15.5N Gourma (AMMA Francoise Guichard)**
112	**2.5**	**18**	**2.5 18N (AMMA Francoise Guichard)**
113	**2.5**	**20.5**	**2.5 20.5N (AMMA Francoise Guichard)**
114	**5.5**	**23**	**5.5 23 N Tamanrasset (AMMA Francoise Guichard)**
115	**-17**	**15**	**-17. 15N Dakar (AMMA Francoise Guichard)**
116	-165	76	165W 76N Location of SHEBA IceBreaker May 1998 (Stephen Klein)
117	128.9	71.6	Tiksi Russia 71.6 N 128.9 - Location of NOAA SEARCH Site (Stephen Klein)
118	110	88	Central Arctic Ocean Point midway between Svalbard & SHEBA (Stephen Klein)
119	**123.2**	**-75.1**	**Antarctica Plateau Dome C: 75 1 S 123 2 E (S. Bony/Christophe Genthon)**
120	**-59.43**	**13.16**	**Barbados 59.43W 13.16N (Optional extra for CFMIP2) (Louise Nuijens)**

Table 2: CMIP5/CFMIP-2 GCM experiments with time series data available.

AGCM	AMIP	AMIP4xCO2	AmipFuture	Amip4K
CNRM-CM5	✓		✓	✓
CanAM4	✓		✓	✓
HadGEM2-A	✓	✓	✓	✓
IPSL-CM5A-LR	✓	✓		✓
EC-EARTH	✓		✓	✓
MPI-ESM-LR	✓	✓		✓
MRI-CGCM3	✓	✓	✓	✓
BCC-CSM-1	✓			
Number of models	8	4	5	7